energies

MDPI

Article

Performance Study of Hybrid Magnetic Coupler Based on Magneto Thermal Coupled Analysis

Shuang Wang [1], Yongcun Guo [1,*], Gang Cheng [1,2] and Deyong Li [1]

1 Anhui Mining Machinery and Electrical Equipment Collaborative Innovation Center, Anhui University of Science and Technology, Huainan 232001, China; shuangw094@126.com (S.W.); gang740@126.com (G.C.); lidy@aust.edu.cn (D.L.)
2 Hefei Institute of Material Science, Chinese Academy of Sciences, Hefei 230000, China
* Correspondence: ldyziyou@126.com; Tel.: +86-0554-6668000

Academic Editor: Tomonobu Senjyu
Received: 3 July 2017; Accepted: 1 August 2017; Published: 4 August 2017

Abstract: Specific to a problem of large vibro-impact aris ing from the cutting unit of the hard rock tunnel boring machine (TBM), a hybrid magnetic coupler based on soft start was proposed in this paper. The mathematical model for total eddy current losses of such a coupler was established by field-circuit method. Then, magnetic-thermal coupling simulation was performed by virtue of three-dimensional finite element software. In addition, an experimental prototype was independently designed; by comparing the model with experimental data, validity of the above mathematical model was verified. The relevant research results indicated that calculated values were consistent with experimental values, and the magneto thermal coupling method could be applied to accurately analyze temperature distribution of the hybrid magnetic coupler. By contrast to the existing magnetic coupling of the same dimension, output efficiency of the hybrid magnetic coupler was improved by 1.2%. Therefore, this research technique can provide references for designing the cutting unit of hard rock TBM with a high start impact.

Keywords: hybrid magnetic coupler; magneto thermal coupling; output efficiency; total eddy current loss

1. Introduction

The cutting unit serves as a core component of the hard rock tunnel boring machine (TBM), and thus its performance has a direct influence on structural strength and service life of the TBM [1–3]. In order to improve the performance of such a cutting unit, soft start technology can be adopted [4] to reduce vibro-impact and cutting pick wear at the time of tunneling, extend the service life of the cutting pick, and improve the corresponding tunneling efficiency [5].

A coupler based on magnetic driving technology is a kind of novel speed control equipment [6] which features light load starting, overload protection, vibration isolation, etc. [7]. As a result, it has attracted extensive attention at home and abroad. Magnetic sources of the magnetic coupler can be either permanent magnets or electromagnetic devices.

The existing magnetic coupler can be roughly divided into three types, such as the vertical barrel magnetic coupler [8], the axial disc magnetic coupler [9], and the cage-shaped asynchronous magnetic coupler [10]. While Sun Zhongsheng et al. perform an in-depth study on the magnetic field and mechanical characteristics of the permanent magnet governor of a barrel structure [11], Zhang Meng et al. probe into speed control performance and energetic efficiency of the vertical flux permanent magnetic coupling [12]. In addition, Zhang Hongjun et al. simulate starting and decoupling processes of the magnetic coupling so that the judging criteria for simple starting and decoupling are verified [13]. Based on an analytical method, Kim et al. propose linear coupling characteristics for barrel magnetic couplers [14]. Two-dimensional (2D) magnetic field distribution of the axial disc magnetic coupler was improved by Wang et al. [15]. Budhia et al. put forward a double-disc magnetic coupler and took advantage of its structural symmetry to balance the axial force [16]. Optimal design was carried out by Mohammadi et al. for a single/double-disc magnetic eddy-current coupler in combination with the conventional Faraday's law of electromagnetic induction and Ampere's law, based on which an analytical model that can be adopted to deal with complex geometry and material performance is further proposed [17]. Ge Yanjun et al. established an output torque model for the asynchronous magnetic coupler of a permanent magnet type and figured out various defects related to the leakage coefficient of such a coupler according to a magnetic circuit method, a finite element method, and a line of magnetic force-based closed-circuit methods [18].

In allusion to the above shortcomings, a hybrid magnetic coupler is presented in this paper. Combining the traditional barrel magnetic coupler and the double plate magnetic coupler, not only did the area of the induced magnetic field increase, but magnetizing could be performed both axially and radially to improve the corresponding propagation efficiency. Moreover, a total eddy current loss model was set up for such a type of magnetic coupler to compare the output efficiency between it and the general double plate magnetic couplers. Hence, the validity of the total eddy current loss model was verified by independently designed tests. This study aims at lowering starting vibro-impact of the TBM cutting unit and to provide protection for such a cutting unit under the circumstance of regular overload.

2. Air Gap Flux Density Model

In combination with structural features of the existing magnetic coupler, a hybrid magnetic coupler is presented in this paper, and magnetizing of its axial and radial permanent magnets could be carried out simultaneously. In addition, a copper conductor cut the magnetic line of force in the radial direction and on its end face to increase electromagnetic damping. In this way, transmission power could be substantially improved in a condition of identical volume or size; moreover, in the case that the transmission power was at a certain value, both volume and size of such a coupler could be reduced to decrease the space it occupied. The schematic diagram of hybrid magnetic coupler is shown in Figure 1a.

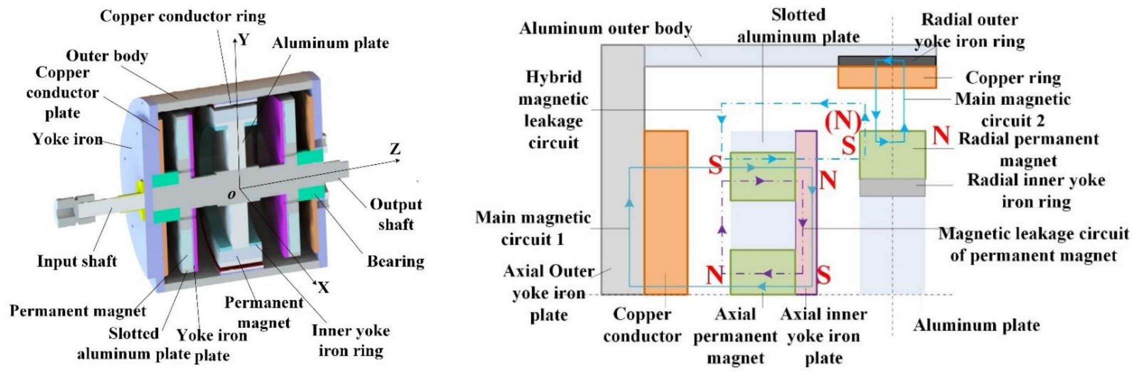

(**a**) (**b**)

Figure 1. Hybrid magnetic coupler: (**a**) Schematic diagram of hybrid magnetic coupler; (**b**) Magnetic circuit diagram of hybrid magnetic coupler.

Considering that the hybrid magnetic coupler was equipped with a structure of bilateral symmetry, 1/4 of it was adopted to perform magnetic circuit analysis for the purpose of analysis simplification. In Figure 1b, a magnetic line of force chart is given for the hybrid magnetic coupler. Compared to the ordinary barrel magnetic coupler or disc magnetic coupler, it had a more sophisticated flux path that was constituted by a main magnetic circuit, an air gap leakage circuit, hybrid leakage circuit, and slot leakage circuit. Concerning most magnetic lines of force, a path of low magnetic resistance was selected, and the line passed through the air gap, copper disc, and yoke to form the main magnetic circuit including the main magnetic circuit 1 and the magnetic circuit 2. Regarding a small number of magnetic lines of force circuits directly through the air gap or adjacent to the permanent magnet, they were referred to as magnetic flux leakage that could not be cut by a rotary copper conductor. Besides, magnetic flux leakage was divided into air gap leakage circuit, hybrid leakage circuit, and slot leakage circuit. Among them, the air gap leakage circuit changed together with variations in the length of the air gap; the slot leakage was associated with the number of permanent magnets arranged; and the hybrid leakage stemmed from the magnetic line of force circuit between one permanent magnet in an aluminum groove and the other permanent magnet in an aluminum dish. Additionally, a magnetic isolating device could be added to reduce hybrid leakage.

3. Equivalent Magnetic Circuit Model

Figure 2 is an equivalent magnetic circuit diagram of a pair of external magnetic circuits under the pole when the hybrid magnetic coupler is with load. In the case that the hybrid magnetic coupler with load is running in a steady state, eddy currents generated in the copper conductor tend to become stable and their directions change alternatively. Depending on Lenz's law, the magnetic field of the induced currents is required to impede changes in the original flux so that the magnetic field incurred by it, exerts an action contrary to that of the original magnetic field produced by the permanent magnet. As a result, a magnetomotive force of eddy currents takes form in the magnetic circuit and it is denoted as F_a (unit: A).

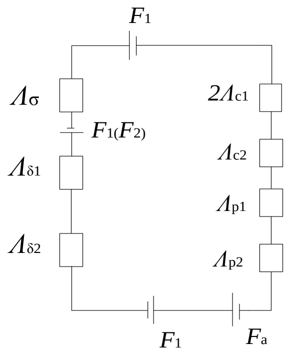

Figure 2. Equivalent magnetic circuit diagram.

In Figure 2, F_1 refers to the equivalent magnetic potential (A) provided by permanent magnets on each axial pole externally, and F_2 refers to the equivalent magnetic potential (A) provided by permanent magnets on each radial pole externally. As direction and length of polarization were set to being equal as far as axial and radial permanent magnets were concerned, it could be deemed that F_1 was approximate to F_2. In addition, Λ_σ is hybrid leakage permeance (H); Λ_{p1} is the magnetic permeance of axial the permanent magnet (H); Λ_{p2} is the magnetic permeance of the radial permanent magnet (H); Λ_{c1} is the magnetic permeance of the axial copper plate (H); Λ_{c2} is the magnetic permeance of the radial copper plate (H); $\Lambda_{\delta 1}$ is the magnetic permeance of the axial air gap (H); and $\Lambda_{\delta 2}$ is the magnetic permeance of the radial air gap (H).

The total magnetic potential difference of the external magnetic circuits ΣF equals the sum of the magnetic potential differences among all parts of the magnetic circuit, that is,

$$\Sigma F = 2F_{c1} + F_{c2} + F_{p1} + F_{p2} + F_\sigma + 2F_{\delta 1} + F_{\delta 2} \tag{1}$$

wherein F_{c1} refers to the magnetic potential difference between axial copper plates (A); F_{c2} refers to the magnetic potential difference between radial copper rings; F_{p1} and F_{p2} refer to the magnetic potential difference between the axial permanent magnets and between the radial permanent magnets, respectively (A); F_σ refers to hybrid magnetic potential difference (A); $F_{\delta 1}$ refers to the magnetic potential difference between axial air gaps (A); $F_{\delta 2}$ refers to the magnetic potential difference between radial air gaps (A).

The main magnetic permeance is composed of the magnetic permeance on all sections of the main magnetic circuit. If magnetic permeance of the hybrid magnetic coupler is expressed in Λ (H), then,

$$\Lambda = \frac{1}{2{\Lambda_{c1}}^{-1}+{\Lambda_{c2}}^{-1}+{\Lambda_{p1}}^{-1}+{\Lambda_{p2}}^{-1}+{\Lambda_{\sigma}}^{-1}+2{\Lambda_{\delta 1}}^{-1}+{\Lambda_{\delta 2}}^{-1}} \tag{2}$$

Therefore, the total magnetomotive force in the magnetic circuit can be written as,

$$F = F_1 - F_a \tag{3}$$

wherein $F_1 = H_C h$ (H_C refers to the coercivity of the permanent magnet (A/m); h refers to the direction of the permanent magnet along the direction of polarization (m); F_a refers to the equivalent magnetomotive force generated by eddy current (A); $F_a = k_e i_e$ (as the coefficient of equivalent conversion, k_e = 1.5–2.5, and equals 2.5 in this paper; i_e refers to the effective eddy current (A)).

According to the magnetic resistance calculation formula, the following equations can be obtained.

$$\Lambda_{p1} = \Lambda_{p2} = \frac{\mu_r S_{pm}}{h} \tag{4}$$

$$\Lambda_{\delta 1} = \frac{\mu_0 S_{pm}}{\delta_1} \tag{5}$$

$$\Lambda_{\delta 2} = \frac{\mu_0 S_{pm}}{\delta_2} \tag{6}$$

$$\Lambda_{c1} = \frac{\mu_0 S_{pm}}{l_1} \tag{7}$$

$$\Lambda_{c2} = \frac{\mu_0 S_{pm}}{l_2} \tag{8}$$

wherein S_{pm} refers to the area of overlap between permanent magnets (mm^2); l_1 refers to the thickness of the axial copper plate (mm); l_2 refers to the thickness of the radial copper ring (mm); $\mu_0 = 4\pi \times 10^{-7}$ refers to air permeability (H/m); and μ_r refers to the relative permeability of the permanent magnet (H/m).

Expressions for Φ_g denoting magnetic flux in the air gap and magnetic flux density B_g are as follows.

$$\Phi_g = \frac{F}{1/\Lambda} = (F_1 - F_a)\left(\frac{2}{\Lambda_{c1}} + \frac{1}{\Lambda_{c2}} + \frac{1}{\Lambda_{p1}} + \frac{1}{\Lambda_{p2}} + \frac{2}{\Lambda_{\sigma}} + \frac{1}{\Lambda_{\delta 1}} + \frac{1}{\Lambda_{\delta 2}}\right) \tag{9}$$

$$B_g = \frac{\Phi_g}{S_{pm}} \tag{10}$$

4. Total Eddy-Current Loss Model

Figure 3 shows equivalent structure diagrams of the copper conductor with (a) axial copper conductors with radii r_1, and r_2 and (b) with radii r_3 and r_4. It is assumed that r_1 and r_2 are outer and inner diameters of an axial copper disc (mm), while r_3 and r_4 are outer and inner diameters of a radial copper ring (mm). The axial copper disc is deemed to be formed by numerous copper bars that have a length of $(r_2 - r_1)$ and pass through the center of a circle, and the radial copper ring is formed by countless copper bars with a length of $(r_4 - r_3)$ and through the center of a circle as well.

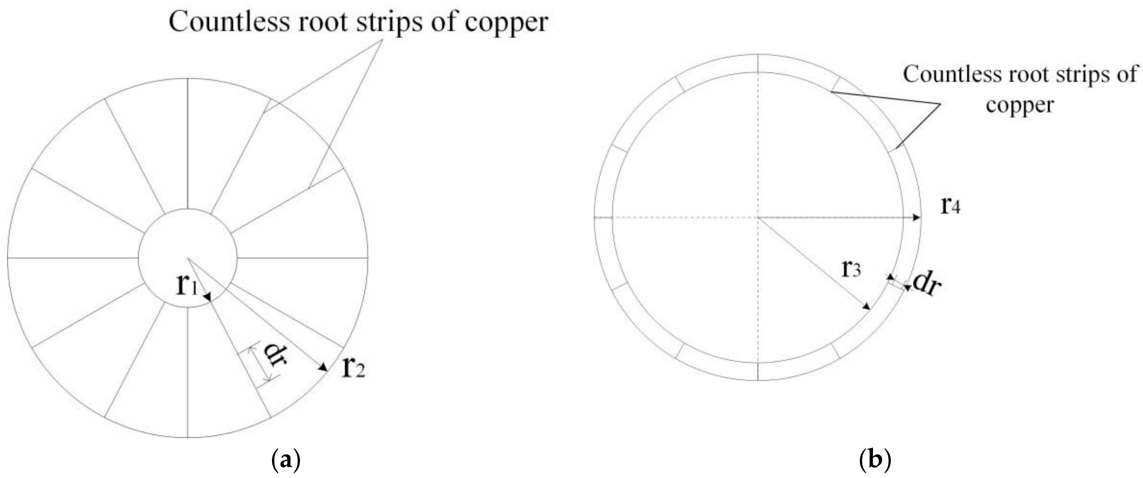

Figure 3. Equivalent structure diagram of copper conductor: (**a**) Axial copper plate; (**b**) Radial copper ring.

The induced electromotive force generated on section dr of the copper bar is expressed in,

$$d\varepsilon = B_g \omega_s \sin(\omega_s t) dr \tag{11}$$

wherein B_g refers to the magnetic flux density in the air gap (T); ω_s refers to the angular velocity of the slip, and $\omega_s = \omega_1 - \omega_2$ (ω_1 and ω_2 respectively refer to the angular velocity of rotation of a copper conductor (or copper ring) and the axial permanent magnet plate (or radial permanent magnet plate).

It is assumed that s is the slip ratio and the calculation formula for it is as follows.

$$s = 2\pi \frac{\omega_1 - \omega_2}{\omega_1} \tag{12}$$

Through transformation, we can obtain

$$\omega_s = 2\pi s n_1 \tag{13}$$

where n_1 is the revolving speed of the loading motor, that is, the input speed in r/m.

Electromotive forces of the axial copper plate (ε_a) and the radial copper ring (ε_r) can be calculated according to the following formulas, separately.

$$\varepsilon_a = \int_{r_1}^{r_2} d\varepsilon = 2\pi s n_1 B_g \sin(2\pi s n_1 t)({r_2}^2 - {r_1}^2)/2 \tag{14}$$

$$\varepsilon_r = \int_{r_3}^{r_4} d\varepsilon = 2\pi s n_1 B_g \sin(2\pi s n_1 t)({r_4}^2 - {r_3}^2)/2 \tag{15}$$

Length of the copper conductor is assumed to be l (mm). Then, considering that conductivity of copper is σ (S/m), resistance for an infinitesimal section dr is expressed in the equation below.

$$dR = \frac{dr}{2\pi\sigma r\Delta} \tag{16}$$

Resistance from r_1 to r_2 on the axial copper disc, corresponding to permanent magnet on each pole, is denoted as $R_{1a,}$ while that from r_3 to r_4 on the corresponding radial copper ring is R_{1r}. Respectively, their equations are presented as follows in (17) and (18).

Δ refers to the skin depth of a copper conductor (mm); N_{pa} refers to the number of axial pole-pairs; N_{pr} refers to the number of radial pole pairs; k_R refers to the correction factor of resistance at different speeds and changes within the range of 0.6–4.6 [17].

A copper conductor is hardly magnetically conductive, so its permeability is approximate to air permeability [18], in which case the skin depth of the axial copper conductor (Δ_a) and the skin depth of the radial copper conductor (Δ_r) are, respectively, equal to Equation (19)

$$R_{1a} = 2k_R N_{pa} \int_{r_1}^{r_2} \frac{dr}{2\pi\sigma l \Delta_a} = \frac{k_R N_{pa}}{\pi\sigma\Delta_a} \ln \frac{r_2}{r_1} \tag{17}$$

$$R_{1r} = 2k_R N_{pr} \int_{r_3}^{r_4} \frac{dr}{2\pi\sigma l \Delta_r} = \frac{k_R N_{pr}}{\pi\sigma\Delta_r} \ln \frac{r_4}{r_3} \tag{18}$$

$$\left.\begin{array}{l} \Delta_a = \left(\mu_0 \sigma N_{pa} \pi s n_1\right)^{-1/2} \\ \Delta_r = \left(\mu_0 \sigma N_{pr} \pi s n_1\right)^{-1/2} \end{array}\right\} \tag{19}$$

Based on the above analysis, it was found that eddy currents generated by permanent magnet under each pole are expressed in Equation (20). I_{1a} refers to the eddy current generated by the axial permanent magnet each pole; I_{1r} refers to the eddy current generated by the radial permanent magnet under a pair of poles.

$$I_{1a} = \frac{\varepsilon_a}{R_a}; I_{1r} = \frac{\varepsilon_r}{R_r} \tag{20}$$

Let B_g be the air gap flux density. By substituting Equations (9) and (15) to (20) into (10), we may obtain the air-gap magnetic flux density

$$B_g = F\left[\frac{1}{\Lambda} S_{pm} + \frac{k_e \pi\sigma\Delta_a \omega_s \sin(\omega_s t)\left(r_2^2 - r_1^2\right)}{2N_{pa} k_R \ln \frac{r_2}{r_1}} + \frac{k_e \pi\sigma\Delta_r \omega_s \sin(\omega_s t)\left(r_4^2 - r_3^2\right)}{2N_{pr} k_R \ln \frac{r_4}{r_3}}\right] \tag{21}$$

P_{sa} refers to the total eddy current loss on the axial copper plate and P_{sr} refers to the total eddy current loss on the radial copper ring. The eddy-current loss on the axial copper plate of each pole (P_{1sa}) is

$$P_{1sa} = I_{1a}^2 R_{1a} \tag{22}$$

The eddy-current loss on the radial copper ring of each pole (P_{1sr}) is

$$P_{1sr} = I_{1r}^2 R_{1r} \tag{23}$$

The total eddy current loss of the complex magnetic coupler (P_s) is calculated as

$$P_S = N_{pr}\, P_{1sr} + N_{pa}\, P_{1sa} \tag{24}$$

5. Eddy-Current Field Simulation Based on Magneto Thermal Coupling Analysis

Three dimensional (3D) hexahedral hot nodes were used to perform thermal analysis on the eddy current field of the hybrid magnetic coupler based on an equivalent thermal network method [19] and the current between one node and any other node was denoted by six thermal resistances. However, the eddy current loss of each node that cannot be directly obtained by the computation structure of the magnetic field is expressed in the average eddy current loss of the entire copper conductor in most cases. As a consequence, the eddy current loss is unable to acquire the correct temperature distribution of such a conductor. In this study, 3D finite element magneto thermal coupling analysis was employed together with Ansoft Maxwell 15.0 (ANSYS, Inc., Canonsburg, PA, USA) and Ansys Workbench 14.0 (ANSYS, Inc., Canonsburg, PA, USA) to construct coupling simulation models for electromagnetic and temperature fields of hybrid magnetic couplers and to analyze the impact of heat generated by eddy currents on the function parameters of the copper conductor disc and the permanent magnet. In addition, thermal power of eddy currents was imported as load of the heat source into the temperature field and the thermal power that was generated by the eddy currents and acted as the load of the heat source were imported successively into a temperature field module of Transient Thermal. In this way, the precise value of temperature could be worked out directly.

In the case that radiation was ignored, a partial differential equation of heat that takes both conduction and convection [20] into account is,

$$\rho c\left(\frac{\partial T}{\partial t} + \boldsymbol{V}^T \boldsymbol{L} T\right) = \boldsymbol{L}^T(\boldsymbol{D}\boldsymbol{L}T) + Q \tag{25}$$

$$\boldsymbol{L} = \begin{pmatrix} \frac{\partial}{\partial x} \\ \frac{\partial}{\partial y} \\ \frac{\partial}{\partial z} \end{pmatrix}, \boldsymbol{V} = \begin{pmatrix} V_x \\ V_y \\ V_z \end{pmatrix}, \boldsymbol{D} = \begin{bmatrix} K_{xx} & & \\ & K_{yy} & \\ & & K_{zz} \end{bmatrix} \tag{26}$$

where ρ refers to density (kg/m^3); c refers to specific heat capacity (J/kg°C); T refers to temperature (°C); V refers to the speed of heat transfer (m/s); $\boldsymbol{D}$ refers to the matrix of heat conductivity; K_{xx}, K_{yy}, and K_{zz} refer to the heat conductivity of the x, y, and z axes, respectively; Q refers to the quantity of heat generated per unit volume (J).

5.1. Combined Simulation Platform Establishment

A combined simulation flowchart for magneto thermal coupling of the hybrid magnetic coupler is presented in Figure 4a, and in Figure 4b, a schematic diagram for coupling of the magnetic coupling module of the hybrid magnetic coupler is presented. Firstly, 3D modeling was conducted for the hybrid magnetic coupler; secondly, the established 3D model was imported into Maxwell Ansoft to carry out a magnetic field simulation to determine eddy current loss power in a condition of the preset slip. Subsequently, the power obtained was used as the load of the heat source and imported into the mechanical transient thermal analysis module, which was followed by analysis according to general procedures of finite element analysis. In the end, temperature distribution of the hybrid magnetic coupler was achieved.

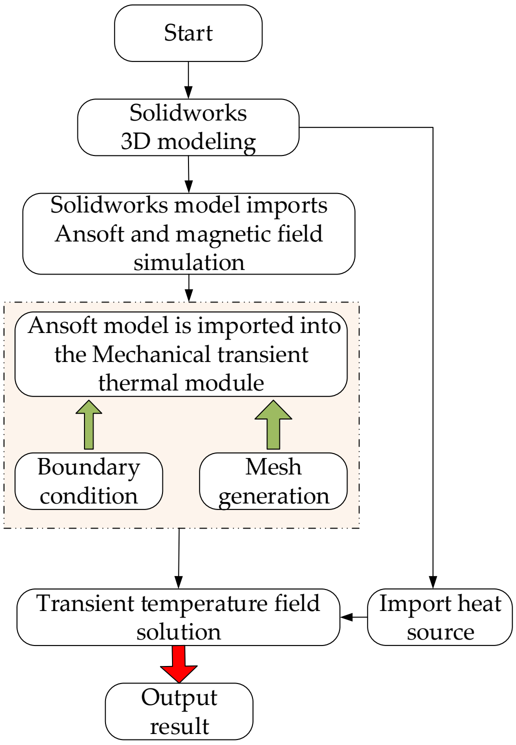

(**a**)

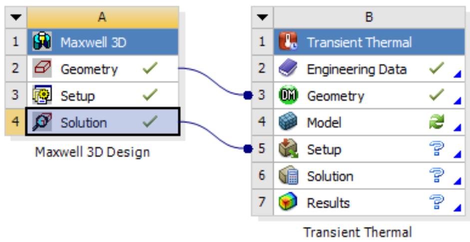

(**b**)

Figure 4. Software Co-simulation: (**a**) Software Co-simulation process; (**b**) Software Co-simulation screenshot.

5.2. Simulation Parameter Setting

According to the parameters of the experimental prototype of the hybrid magnetic coupler shown in Table 1, the 3D magnetic field simulation software Ansoft was used to establish the model, where the solution type was defined as transient electromagnetic field simulation. The material of the permanent magnet was NdFe35, the yoke material of the permanent magnet was steel_1010, the solution time was set as 0.3 s, the step was 0.001 s, and the outer rotor input speed was 450 r/min.

Since the mesh generation directly affects the accuracy of the finite element simulation results, in order to obtain higher mesh generation quality, a selective generation method was adopted, that is, for the copper conductor, yoke, permanent magnet, and the air gap which require relatively high accuracy of solution, the mesh generation should be relatively dense (the number of grid was 35,000), and for other parts which require relatively low accuracy of solution, the mesh generation should be relatively sparse to shorten the simulation time and improve the simulation quality.

Table 1. Dimension parameters of the magnetic coupler.

Parameter	Data	
	Hybrid	**Double**
Axial magnet pole pairs	4	4
Axial magnet rotor outer diameter	200 mm	200 mm
Axial magnet rotor thickness	25.4 mm	25.4 mm
Axial copper conductor outer diameter	200 mm	200 mm
Axial copper conductor thickness	8 mm	8 mm
Axial yoke iron outer diameter	200 mm	200 mm
Axial yoke iron thickness	10 mm	10 mm
Radial magnet pole pairs	4	-
Radial magnet rotor thickness	25.4 mm	-
Radial magnet rotor inner diameter	200 mm	-
Permanent magnet size	50.8 mm × 25.4 mm × 12.7 mm	50.8 mm × 25.4 mm × 12.7 mm

In accordance with the above settings, air gap flux density distribution of two magnetic couplers at diverse rotor positions was acquired through simulation, as shown in Figure 5.

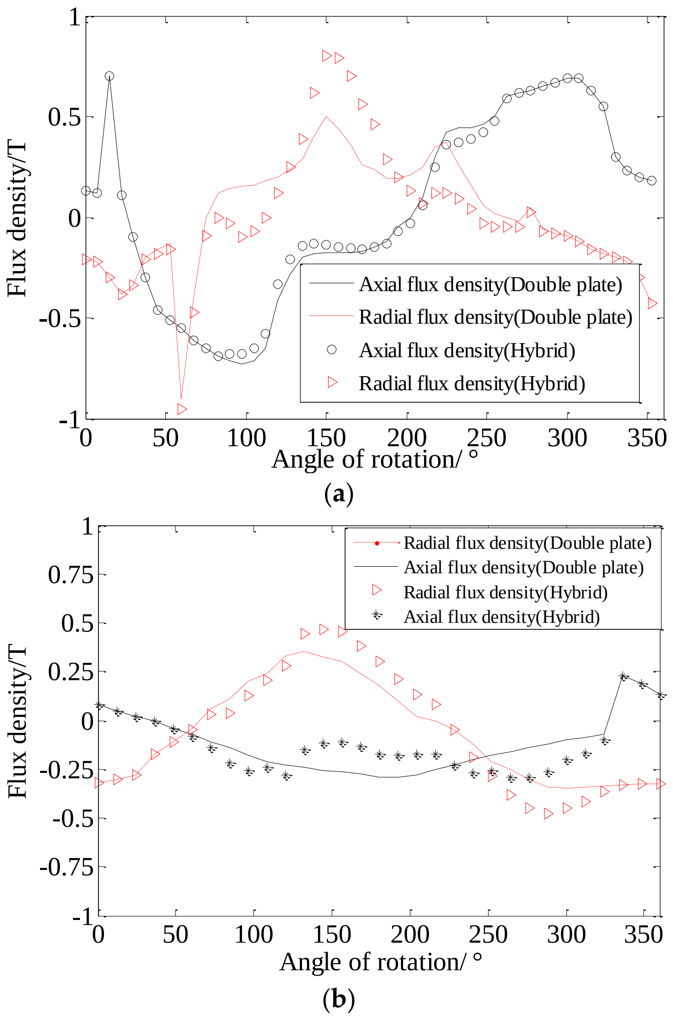

Figure 5. Magnetic flux density distribution at the center of the air gap: (**a**) the radial air gap is 5 mm and the axial air gap is 10 mm; (**b**) the radial air gap is 20 mm and the axial air gap is 15 mm.

It could be found by analyzing Figure 5 that axial magnetic flux densities of air gap fields formed by the hybrid magnetic coupler and the general double-disc magnetic coupler were nearly the same. By contrast, as far as their radial magnetic flux densities were concerned, that of hybrid magnetic coupler was greater than the general double-disc magnetic coupler. The corresponding reason was that existence of the radial permanent magnet rotor in the hybrid magnetic coupler, leading to the rise of an effective overlap area of the magnetic field and the increase in air gap field intensity.

The eddy current loss generated within the permanent magnetic field was then treated as the heat source and imported into the temperature field for simulation; eddy current power simulation results of the hybrid magnetic coupler's permanent magnetic field at the time of the slip equal to 450 r/min are given in Figure 6.

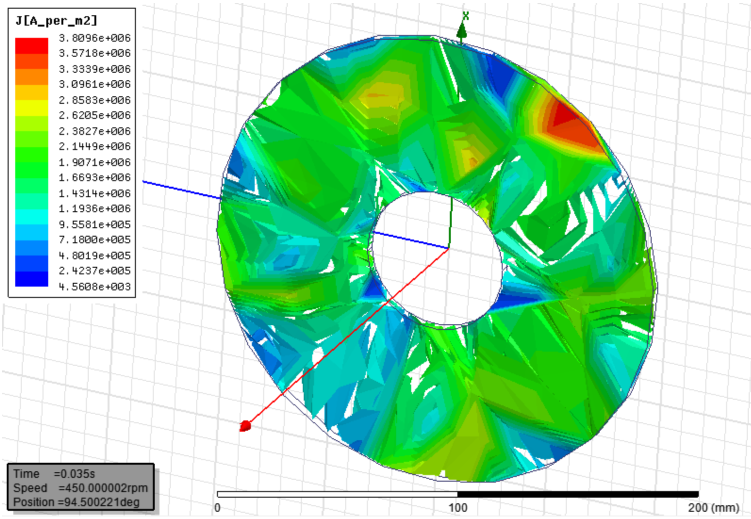

(**a**)

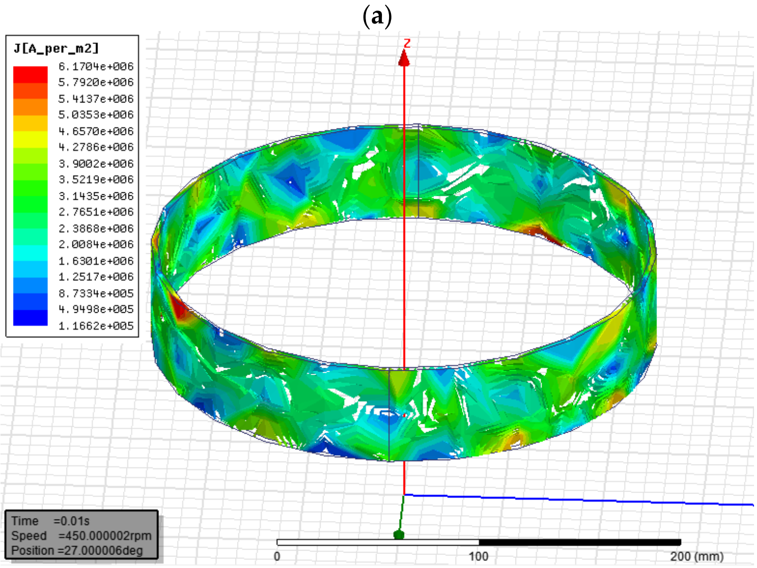

(**b**)

Figure 6. Eddy current loss of copper conductor: (**a**) axial; (**b**) radial.

Furthermore, after the eddy current loss shown in Figure 6 was imported into the temperature field, temperature field simulation results of the copper conductor were those presented in Figure 7. Regarding the axial copper conductor, the maximum temperature takes form in a region where the density of eddy currents arrives at the highest value. Moreover, the area of the maximum temperature of the permanent magnet correspondeds to that of the copper conductor considering that the air gap served as a heat-transfer medium to transmit heat to the permanent magnet. Thermal conductivity (unit: W/(mK)) of materials used by the hybrid magnetic coupler can be described as: 0.027 W/(mK) for air, 220 W/(mK) for aluminum, 20 W/(mK) for the permanent magnet, 40 W/(mK) for iron, 50 W/(mK) for steel, 380 W/(mK) for copper, 0.18 W/(mK) for insulating materials, and 0.5 W/(mK) for glue. In addition, temperature rise fell into the range permitted by the permanent magnet and insulating materials, etc.

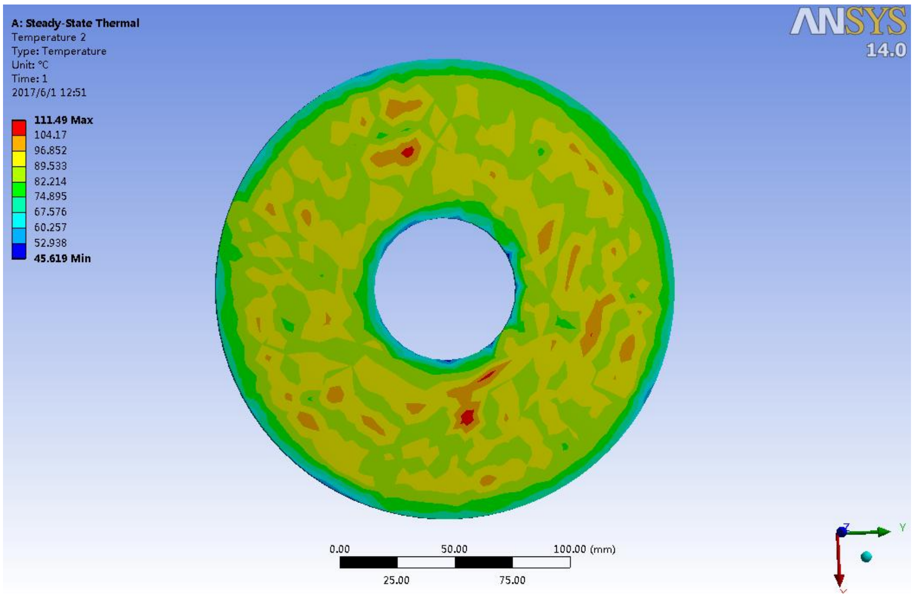

(a)

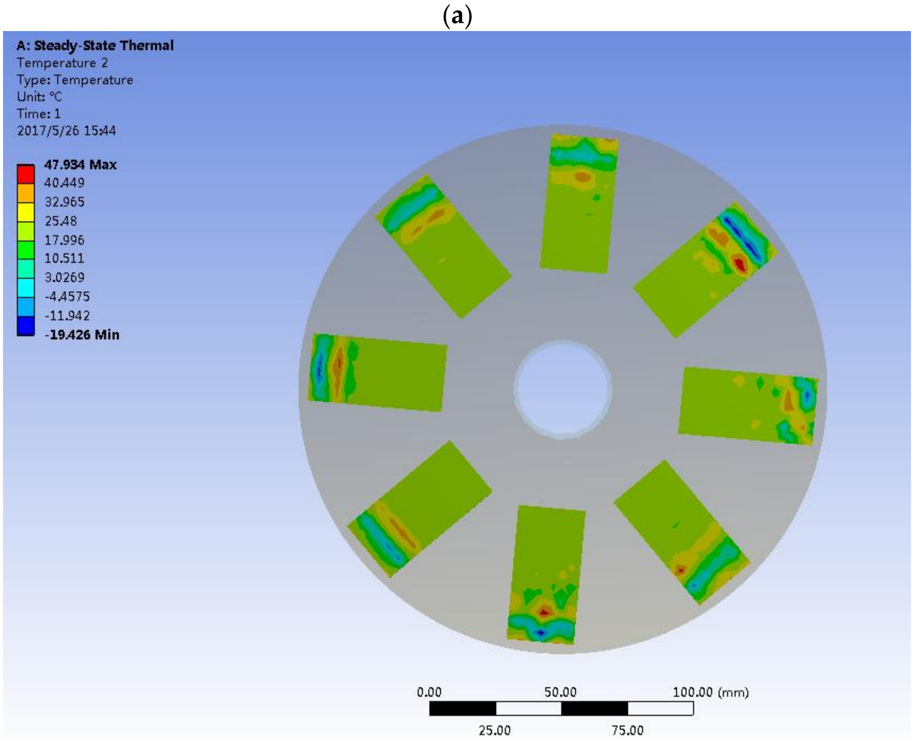

(b)

Figure 7. Axial temperature simulation results: (**a**) The axial temperature distribution of the copper plate; (**b**) Permanent magnet temperature distribution.

6. Experimental Verification

The 1:2 prototype experimental device of the hybrid magnetic coupler is shown in Figure 8. It is mainly composed of the YE2-90S-4 three-phase asynchronous alternating current (AC) motor (with the rated speed of 1400 r/m), frequency converter (with the frequency range of 10 Hz to 50 Hz), YH-502 dynamic torque sensor (with the range capacity of 0 to 500 Nm and the precision of 0.5%, from Beijing Yuhang Instrument Technology Co., Ltd., Beijing, China), the elastic coupler, UX-52 digital-display governor, hybrid magnetic coupler (1:2 prototype), YE2-80L-4 type load motor, WT-10A digital-display gauss meter (with the range of 0 to 2000 mT), and MS6208B non-contact digital-display tachometer.

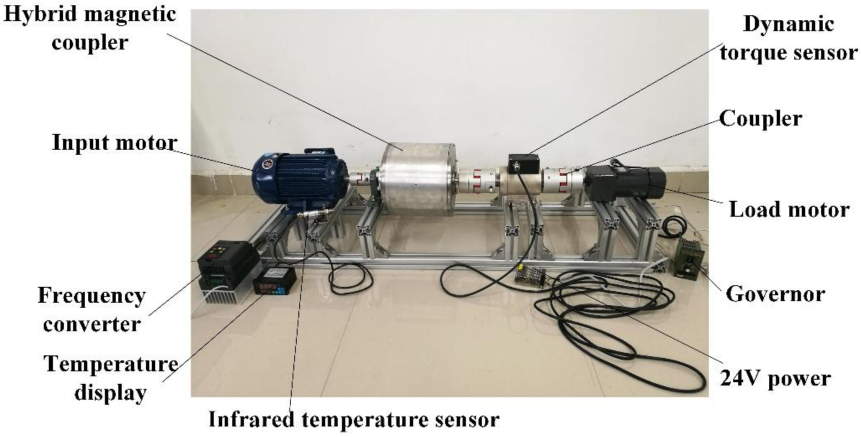

Figure 8. Test prototype diagram.

With regard to the figure of experimental prototypes, the input motor makes use of a frequency convertor to control revolving speed, while the load motor takes advantage of the governor to control the revolving speed. As for the dynamic torque sensor, it performs real-time monitoring on output torque and revolving speed of experimental prototypes and its measuring range is 0 N·m–500 N·m or 0 r/m–6000 r/m.

At the time of the tests, the output shaft of an experimental prototype was connected to one end of the torque sensor by virtue of the elastic coupler; under such a circumstance, the other end of the sensor was connected with the load motor to synchronously rotate together with the motor. For the convenience of data analysis, revolving speed of the load motor turns into a constant of 450 r/m with the help of the governor.

By controlling the revolving speed of the input motor that thus ran at a speed of 50 r/m–450 r/m, the speed input could be measured by a tachymeter. Due to the synchronous revolution of the load motor and the hybrid magnetic coupler, output torque of the experimental prototype was the reading displayed on a torque sensor.

In the first place, the load motor was started non-loaded and entered a stage of smooth running; then, the input motor was started and its revolving speed was gradually changed. The torque sensor was utilized to read and record output torque and revolving speed of the experimental prototype. Besides, a contactless rotational speed meter was also adopted to test the revolving speed value obtained after changing the speed of the input motor and acquiring the stable output revolving speed. Finally, the slip ratio between permanent magnet rotor and the copper conductor rotor of the experimental prototype was calculated according to Equation (13).

Under the circumstance that revolving speed of the input motor was given and identical, the hybrid magnetic coupler and the general double plate magnetic coupler of the same volume and dimension were compared to obtain the corresponding output torque, as shown in Table 2.

Table 2. Comparison data of the output torque test of the hybrid and ordinary double plate magnetic couplers.

Input Motor Speed (r/min)	Ordinary Double Plate A (N.m)	Hybrid B (N.m)	Increase Ratio $C = (B - A)/A$
335	4.4	6.3	43%
340	5.1	7.6	49%
360	6.8	8.7	28%
365	8.2	12.4	51%
380	11.3	13.6	20%
385	12.0	14.6	22%
390	12.7	15.2	20%
420	13.9	16.4	18%
430	15.0	19.1	27%
450	17.2	22.1	28%

In line with Table 2, when input revolving speed of the load motor was given and identical, torque generated by hybrid magnetic coupler was about 30.7% numerically higher than that of the general double-disc magnetic coupler. It signifies that transmission power of the hybrid magnetic coupler with the same volume or dimension can be dramatically improved; in addition, if the transmission power was definite, volume and dimension of the coupler can be reduced to decrease the space it occupies.

Figure 9 is an efficiency comparison chart for prototypes of the hybrid magnetic coupler and the conventional double plate magnetic coupler in the same running conditions. Based on analysis, efficiency of the prototype of the hybrid magnetic coupler featured with a new structure was approximately 1.2% higher than that of the general double plate magnetic coupler. It is well known that the efficiency of an ordinary magnetic coupler is about 97–99%. On this basis, the efficiency of the hybrid magnetic coupler proposed in this paper is about 1.2% of the efficiency of the ordinary double plate magnetic coupler, which means the hybrid magnetic coupler is superior.

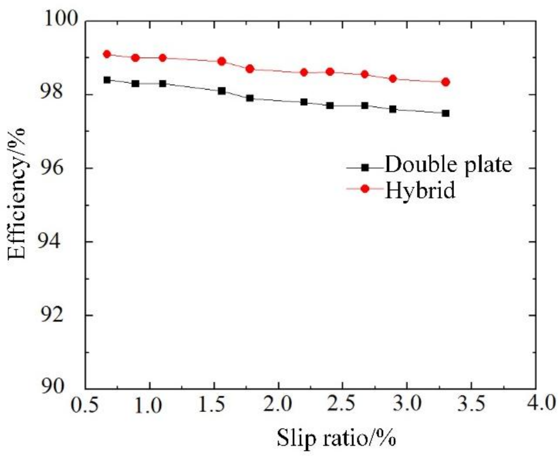

Figure 9. Prototype efficiency comparison chart.

The comparison between calculated and experimental values of the total eddy current loss power is presented in Figure 10. When slip of the experimental prototype is below 250 r/min, calculated and experimental values of the total eddy current loss are not only close to each other, but are almost linear; in addition, their maximum error is 8.5%. If such a slip is 250 r/min, their maximum error is 10.6%, which fundamentally verifies the validity of the model constructed in this paper. As for temperature, it was measured by an infrared thermometer. In the case of a slip equal to 450 r/min, temperature of the axial copper conductor disc was 127.8 °C, slightly higher than its calculated value due to the fact that the actual loss exceeded the calculated loss.

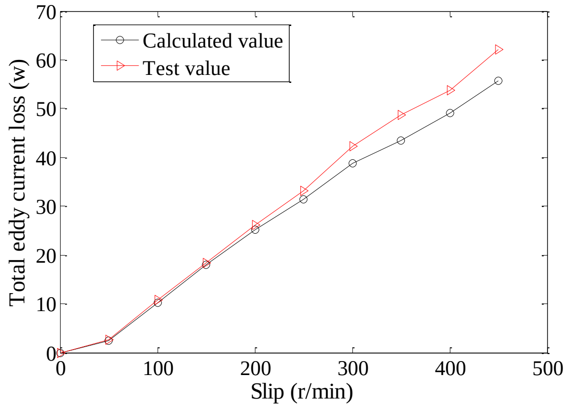

Figure 10. Comparison of calculated values and experimental results for total eddy current losses.

7. Conclusions

Specific to the problem of the high vibro-impact generated by the cutting unit of the hard rock TBM during running, a hybrid magnetic coupler based on soft start was proposed in this paper.

(1) A mathematical model was established for the total eddy current loss of the hybrid magnetic coupler based on a field-circuit method on the one hand; on the other hand, two types of 3D finite element software including ANSYS workbench and ANSOFT Maxwell were adopted to perform magneto thermal coupling simulations.

(2) In combination with concrete structural features of the hybrid magnetic coupler, a prototype was designed and manufactured. In a condition of the same inputs for revolving speed and volume given, output torque and transmission efficiency of the hybrid magnetic coupler went up by 30.7% and about 1.2%, respectively, compared with that of the general double plate magnetic coupler. This indicates that transmission efficiency of the hybrid magnetic coupler can be enormously improved under the circumstance of the same volume or dimension, and the volume and dimension of the coupler can be reduced to bring down the occupied space on the premise of the given transmission power.

(3) It was experimentally verified that the error between calculated and experimental values of the total eddy current loss power is rather small (maximum error: 10.6%), which proves that the magneto thermal coupling analysis method proposed in this study can be utilized to accurately analyze temperature distribution of the hybrid magnetic coupler.

Acknowledgments: This research work was supported by the National Natural Science Fund Project (Grant No. 51641501), the Natural science research project of Anhui University (Grant No. KJ2016A199), and the Natural science research project of Anhui University (Grant No. KJ2017A083).

Author Contributions: Shuang Wang and Yongcun Guo conceived and designed the experiments; Gang Cheng performed the experiments; Deyong Li analyzed the data.

Conflicts of Interest: The authors declare no conflict of interest.

Nomenclature

TBM	tunnel boring machine
F_a	magnetomotive force of eddy currents
F_1	equivalent magnetic potential provided by permanent magnets on each axial pole
F_2	equivalent magnetic potential provided by permanent magnets on each radial pole
Λ_σ	hybrid leakage permeance

Λ_{p1}	magnetic permeance of the axial permanent magnet
Λ_{p2}	magnetic permeance of the radial permanent magnet
Λ_{c1}	magnetic permeance of the axial copper plate
Λ_{c2}	magnetic permeance of the radial copper plate
$\Lambda_{\delta 1}$	magnetic permeance of the axial air gap
$\Lambda_{\delta 2}$	magnetic permeance of the radial air gap
ΣF	the total magnetic potential difference of the external magnetic circuits
F_{c1}	magnetic potential difference between axial copper plates
F_{c2}	magnetic potential difference between radial copper rings
F_{p1}	magnetic potential difference between axial permanent magnets
F_{p2}	magnetic potential difference between radial permanent magnets
F_{σ}	hybrid magnetic potential difference
$F_{\delta 1}$	magnetic potential difference between the axial air gaps
$F_{\delta 2}$	magnetic potential difference between the radial air gaps
Λ	permeance of the external magnetic circuit of the hybrid magnetic coupler
H_C	the coercivity of the permanent magnet
h	the direction of permanent magnet along the direction of polarization
F_a	the equivalent magnetomotive force generated by the eddy current
k_e	the coefficient of equivalent conversion
i_e	the effective eddy current
S_{pm}	the area of overlap between permanent magnets
l_1	the thickness of the axial copper plate
l_2	the thickness of the radial copper ring
μ_0	air permeability
μ_r	the relative permeability of the permanent magnet
Φ_g	magnetic flux in the air gap
B_g	magnetic flux density in the air gap
r_1	refers to the inner diameter of the axial copper plate
r_2	refers to the outer diameter of the axial copper plate
r_3	refers to the inner diameter of the radial copper plate
r_4	refers to the outer diameter of the radial copper plate
R_{1a}	resistance of the permanent magnet of each pole from r_1 to r_2 on the corresponding axial copper plate
R_{1r}	resistance of the permanent magnet of each pole from r_1 to r_2 on the corresponding radial copper plate
Δ	the skin depth of a copper conductor
N_{pa}	the number of axial pole-pairs
N_{pr}	the number of radial pole pairs
k_R	the correction factor of resistance at different speeds and changes
Δ_a	skin depth of the axial copper conductor
Δ_r	skin depth of the radial copper conductor
P_{sa}	the total eddy current loss on the axial copper plate
P_{sr}	the total eddy current loss on the radial copper ring
P_{1sa}	the total eddy current loss on the axial copper plate of each pole
P_{1sr}	the total eddy current loss on the radial copper ring of each pole
P_s	the total eddy current loss of the complex magnetic coupler

ω_1	the angular velocity of rotation of a copper conductor and axial permanent magnet plate
ω_2	the angular velocity of rotation of a copper ring and radial permanent magnet plate
n_1	revolving speed of loading motor, that is, the input speed
l	length of the copper conductor
σ	conductivity of copper
ε_a	electromotive forces of the axial copper plate
ε_r	electromotive forces of the radial copper plate
I_{1a}	the eddy current generated by the axial permanent magnet of each pole
I_{1r}	the eddy current generated by the radial permanent magnet of each pole

References

1. Lin, L.; Mao, Q.; Xia, Y.; Zhu, Z.; Yang, D.; Guo, B.; Lan, H. Experimental Study of Specific Matching Characteristics of Tunnel Boring Machine Cutter Ring Properties and Rock. *Wear* **2017**, *378*, 1–10. [CrossRef]
2. Rostami, J. Performance prediction of hard rock Tunnel Boring Machines (TBMs) in difficult ground. *Tunn. Undergr. Space Technol.* **2016**, *57*, 173–182. [CrossRef]
3. Filbà, M.; Salvany, J.M.; Jubany, J.; Carrasco, L. Tunnel boring machine collision with an ancient boulder beach during the excavation of the Barcelona city subway L10 line: A case of adverse geology and resulting engineering solutions. *Eng. Geol.* **2016**, *200*, 31–46. [CrossRef]
4. Meda, A.; Rinaldi, Z.; Caratelli, A.; Cignitti, F. Experimental investigation on precast tunnel segments under TBM thrust action. *Eng. Struct.* **2016**, *119*, 174–185. [CrossRef]
5. Bouayad, D.; Emeriault, F.; Maza, M. Assessment of ground surface displacements induced by an earth pressure balance shield tunneling using partial least squares regression. *Environ. Earth Sci.* **2015**, *73*, 7603–7616. [CrossRef]
6. Merdzan, M.; Jumayev, S.; Borisavljevic, A.; Boynov, K.O.; Paulides, J.J.H.; Lomonova, E.A. Electrical and Magnetic Model Coupling of Permanent Magnet Machines Based on the Harmonic Analysis. *IEEE Trans. Magn.* **2015**, *51*, 1–9. [CrossRef]
7. Sun, Z.; Zhou, L.; Wang, X.; Huang, Z. Magnetic Field Analysis and Characteristics Research of Cylindrical Permanent Magnet Adjustable Speed Drive. *China Mech. Eng.* **2015**, *26*, 1742–1747.
8. Zhang, M.; Zhao, H.; Liu, X.; Yao, P.; Zhou, Q. Experimental Efficiency Characteristics of Permanent Magnetic Coupling with radial Flux. *Mot. Control Appl.* **2014**, *41*, 52–56.
9. Zhang, H.; Bao, Li.; Li, X. Starting behavior research of coaxial cylinder magnetic coupler. *J. Eng. Des.* **2012**, *19*, 489–493.
10. Kim, J.-M.; Choi, J.-Y.; Koo, M.-M.; Shin, H.-J.; Lee, S.-H. Characteristic Analysis of Tubular-Type Permanent-Magnet Linear Magnetic Coupling Based on Analytical Magnetic Field Calculations. *IEEE Trans. Appl. Supercond.* **2016**, *26*, 1–5. [CrossRef]
11. Wang, J.; Lin, H.; Fang, S.; Huang, Y. A General Analytical Model of Permanent Magnet Eddy Current Couplings. *IEEE Trans. Magn.* **2014**, *50*, 1–9. [CrossRef]
12. Budhia, M.; Boys, J.T.; Covic, G.A.; Huang, C. Development of a Single-Sided Flux Magnetic Coupler for Electric Vehicle IPT Charging Systems. *IEEE Trans Ind. Electron.* **2013**, *60*, 318–328. [CrossRef]
13. Mohammadi, S.; Mirsalim, M. Design optimization of double-sided permanent-magnet radial-flux eddy-current couplers. *Electr. Power Syst. Res.* **2014**, *108*, 282–292. [CrossRef]
14. Ge, Y.; Yuan, Z.; Jia, F.; Yang, J.; Zhou, K. Mechanical properties and testing for squirrel cage asynchronous magnetic coupler. *Trans. Chin. Soc. Agric. Eng.* **2016**, *32*, 68–74.
15. Ge, Y.; Shi, Y.; Jia, F.; Wen, Z. Leakage Coefficient Computation of Permanent Magnetic Asynchronous Coupling. *Mach. Des. Manuf.* **2013**, *1*, 67–70.
16. Yang, C.; Kong, L.; Zhang, T.; Lü, L.; Luo, Y.; Chen, Z. Research on 3D Air-gap Magnetic Field of Field Modulated Asynchronous Magnetic Couplings. *J. Mech. Eng.* **2016**, *52*, 8–15. [CrossRef]
17. Yan, D.; Liu, R.; Hu, M.; Han, J. A New Method to Deal with the Motion Problem in Electromagnetic Field Finite Element Analysis. *Proc. CSEE* **2003**, *23*, 163–167.

18. Deng, Y.; Chen, G.; Yang, X. Algorithm Study of Eliminating Calculation Errors in Large Strain Measurement with Strain Gauges. *J. Exp. Mech.* **2008**, *23*, 227–233.
19. Guo, Y.G.; Zhu, J.G.; Wu, W. Thermal analysis of soft magnetic composite motors using a hybrid model with distributed heat sources. *IEEE Trans. Magn.* **2005**, *41*, 2124–2128.
20. Broadbridge, P.; Ivanova, N.M. Solutions and reductions for radiative energy transport in laser-heated plasma. *J. Math. Phys.* **2015**, *56*, 353–368. [CrossRef]